Article

Atomic-Scale Control of Coherent Thermal Radiation

Bo Zhao, Jung-Hwan Song, Mark Brongersma,* and Shanhui Fan*

Cite This: *ACS Photonics* 2021, 8, 872−878

Read Online

ACCESS | Metrics & More | Article Recommendations | Supporting Information

ABSTRACT: Controlling the temporal coherence of thermal radiation plays an important role in energy harvesting and thermal management. Conventional approaches for thermal radiation control rely on resonances in bulk thermal emitters, which usually have a large footprint and display little tunability. In this work, we explore the possibility to control coherent thermal emission with atomically thin emitters. We show that, despite the atomic thickness, the peak emissivity of these emitters could be as high as the bulk emitters. We identify several linear scaling laws for the radiative properties of atomic-scale systems, providing a pathway for controlling thermal radiation with atomic precision.

KEYWORDS: *hexagonal boron nitride, graphene, coupled-mode theory, surface conductivity, two-dimensional materials*
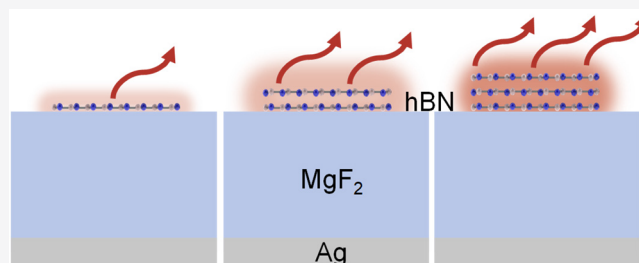
Originating from random charge fluctuations, thermal radiation is usually incoherent in both the spatial and the temporal domains.[1] However, the coherence of thermal radiation, especially the temporal coherence, can be significantly improved using judiciously patterned nanostructures.[2,3] This can be utilized to improve the performance of energy harvesting and thermal management systems that harness thermal radiation for energy transport.[4,5] The spectral and angular properties of thermal radiation are typically controlled by bulk emitters with feature sizes comparable or somewhat smaller than the relevant thermal wavelengths, such as photonic crystals and multilayer structures.[6−9] While such bulk thermal emitters provide plentiful bulk modes for thermal radiation control, low-dimension emitters such as these constructed with two-dimensional (2D) materials can often leverage a high modal density around strong materials resonances. They also offer new degrees of freedom to dynamically control thermal radiation, including the use of strain[10] and electrical gating.[11]

In this work, we explore the control of temporally coherent thermal radiation at the atomic scale with 2D materials. In particular, we focus on using hexagonal boron nitride (hBN), which has a strong high-temperature phonon-polaritonic response in the mid-infrared spectral range.[12] We show that, despite its atomic-scale thickness, thermal emitters made from single or a few atomic layers of hBN can generate a coherent emissivity spectrum with a peak emissivity comparable to bulk materials. The spectral emissivity peak of phononic 2D-material emitters exhibits a much higher quality factor compared to the emissivity peak from emitters based on plasmonic 2D materials like graphene. We show that the radiative properties of the considered hBN thermal emitters depend sensitively on the number of atomic layers. Thus, this

system provides a pathway to achieve atomic-scale control of thermal radiation.

We consider a nanophotonic thermal emitter, as illustrated in Figure 1. The emitter consists of an atomically thin hBN layer on the top, with a MgF$_2$ dielectric spacer, and a substrate made of silver (Ag). The number of the hBN layers is denoted as N. Each layer of hBN has a thickness of $a = 0.34$ nm, and therefore the thickness of the hBN layer is Na. We model the optical properties of hBN layer using a bulk model with two mid-infrared Reststrahlen bands linked to the presence of optical phonon modes in the mid-infrared range. The in-plane phonon modes ($\omega_{TO,\perp} = 1370$ cm^{-1} and $\omega_{LO,\perp} = 1610$ cm^{-1}) and out-of-plane phonon modes ($\omega_{TO,\parallel} = 780$ cm^{-1} and $\omega_{LO,\parallel} = 830$ cm^{-1}) contribute to the in-plane and out-of-plane dielectric functions, respectively:[13,14]

$$\varepsilon_\xi = \varepsilon_{\infty,\xi}\left(1 + \frac{\omega_{LO,\xi}^2 - \omega_{TO,\xi}^2}{\omega_{TO,\xi}^2 - i\gamma_\xi\omega - \omega^2}\right) \quad (1)$$

where $\xi = \parallel, \perp$, and ω is the angular frequency. The other parameters used are $\varepsilon_{\infty,\parallel} = 2.95$, $\gamma_\parallel = 4$ cm^{-1}, $\varepsilon_{\infty,\perp} = 4.87$, and $\gamma_\perp = 5$ cm^{-1}. The dielectric function of Ag is obtained based on a Drude model[15] and the MgF$_2$ is based on literature data.[16] We consider the thermal emission of transverse magnetic (TM) waves (*H*-field polarized in the *y* direction) in the
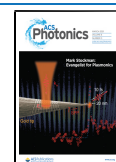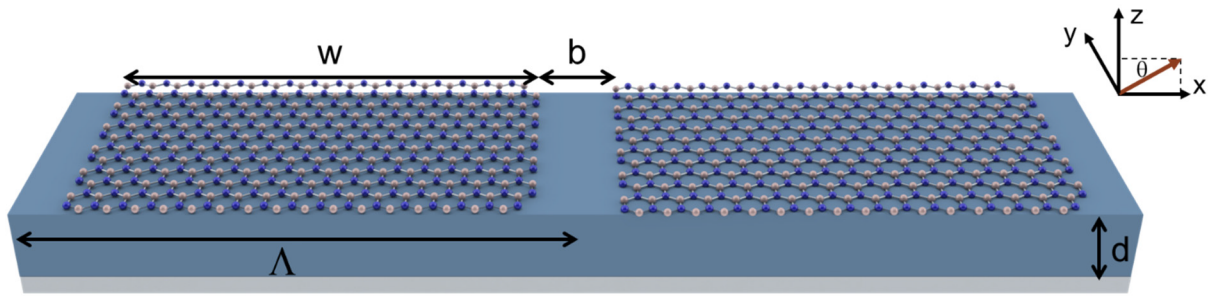
Figure 1. Schematic of the considered thermal emitter with an atomically thin hBN top layer. The number of hBN layers are denoted as N. This layer is patterned to be periodic in the x-direction with a periodicity Λ. The hBN ribbons have a uniform width w with a spacing b. The middle layer (light blue) and the substrate (silvery) are MgF_2 and Ag films, respectively. The thickness of MgF_2 is d, and the Ag substrate is assumed to be infinitely thick.
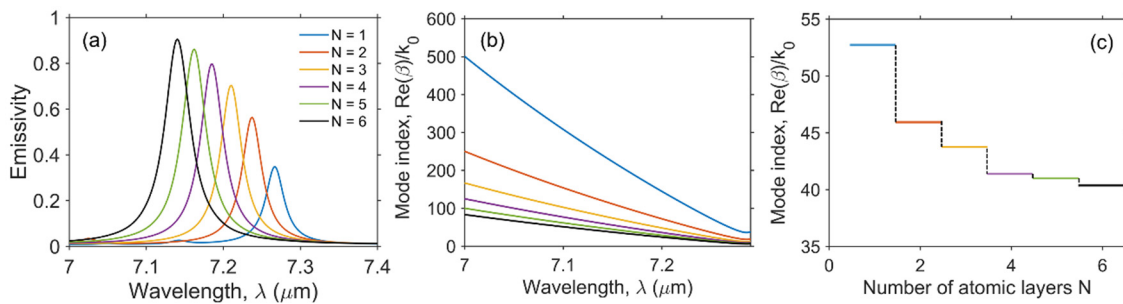

Figure 2. (a) Emissivity spectra in the normal direction for the thermal emitters with different number of hBN atomic layers (N). For all cases, we use $d = 1.4$ μm, $\Lambda = 0.05$ μm, and $w = 0.04$ μm. (b) Mode index of the phonon polaritons in thin hBN film with different numbers of atomic layers. The mode index is obtained based on eq 2. (c) Mode index of the ribbon mode at the peak emissivity for emitters with different numbers of atomic layers.

normal direction. Based on Kirchhoff's law and energy balance,[17] we compute the spectral emissivity (ε_λ) from the spectral absorptivity (α_λ) as $\varepsilon_\lambda = \alpha_\lambda = 1 - R_\lambda$, where R_λ is the spectral reflectivity and λ is the wavelength.

The phonon modes of hBN notably impact the optical properties and thus provide an opportunity to tailor the thermal emission spectrum. Since the damping coefficients γ are rather small, the dielectric function becomes negative between the TO and LO phonon modes (see Supporting Information for plots of the dielectric function), and the material loss is negligibly small except near the TO phonon frequency. The low-loss properties allow us to harness the phonon polaritons in hBN.[18] We note that, although our emitter structure is similar to the metal−insulator−metal structure, the fundamental mode responsible for the coherent emission here is not the same as in the conventional metal−insulator−metal structures since the top hBN layer is far thinner than the typical metal layer used.[19] Because of the atomic thickness of the hBN resonator, although the dielectric function of hBN is anisotropic or hyperbolic, the dielectric function in the z direction plays a negligible role for the case we studied in this work. Therefore, we focus on the Reststrahlen band of the in-plane phonon modes, which are indicated with two white-dashed horizontal lines on the contour plots throughout the paper. Using the dielectric function of hBN, one can describe the dispersion of the fundamental order of the phonon polariton in the atomically thin hBN with a similar approach used for the surface plasmon polariton of graphene:[15]

$$\frac{\varepsilon_1}{\sqrt{\beta^2 - \varepsilon_1 k_0^2}} + \frac{\varepsilon_2}{\sqrt{\beta^2 - \varepsilon_2 k_0^2}} = -\frac{i\sigma_{hBN}}{\omega\varepsilon_0} \quad (2)$$

where $k_0 = \omega/c_0$ is the vacuum wave vector with c_0 being the light speed in vacuum, β is the wave vector for the phonon polariton in hBN, ε_0 is the permittivity of vacuum, ε_1 and ε_2 are the dielectric functions of the media that are on either side of hBN, and σ_{hBN} is the equivalent surface conductivity of hBN, which is connected to its dielectric function as[20]

$$\varepsilon_\perp = 1 + i\frac{\sigma_{hBN}}{\varepsilon_0 \omega N a} \quad (3)$$

For later use, we also define the mode index $n \equiv \frac{c_0\beta}{\omega}$. In this work, we focus on utilizing the phonon polariton resonances in the hBN ribbons to tailor the emissivity spectrum. The condition for the ribbon resonance can be described by a Fabry-Pérot model:[15,21−25]

$$\Delta\varphi + \text{Re}(\beta)w = m\pi \quad (4)$$

where the integer m denotes the resonance order and $\Delta\varphi$ is the phase acquisition at the edge of the ribbon. In the Supporting Information, we show that the predictions from eq 4 agree very well with the direct computation results for hBN ribbon emitters.

Based on the ribbon resonances, we obtain a coherent emissivity spectrum for emitters with different layers of hBN, as shown in Figure 2a. For the monolayer hBN resonator, the peak emissivity can reach as high as 0.35, which is quite significant considering its atomic-scale thickness. As a comparison, the emissivity in the normal direction at off-resonance wavelength of 7.2 μm is only 0.0025 for a suspended

continuous hBN monolayer. Thus, the use of the ribbon structure plays a significant role in enhancing emissivity. When the number of hBN layers increases, the peak emissivity increases significantly as well, highlighting the possibility of achieving atomic-level control. The high sensitivity comes from the fact that, in the designed emitters, the Ag substrate is quite conductive and MgF$_2$ is essentially transparent in the mid-infrared range we considered here. Therefore, the thermal emission from our emitter system is dominated by the hBN layer. We can improve our understanding of the atomic-scale sensitivity of the emissivity spectrum to the hBN layer thickness from temporal coupled-mode theory, which predicts the spectral absorptivity or the spectral emissivity near the ribbon resonances as[26−28]

$$\varepsilon_\omega = \frac{4\gamma_i\gamma_r}{(\omega - \omega_0)^2 + (\gamma_i + \gamma_r)^2} \tag{5}$$

where ω_0 is the resonant frequency, γ_r and γ_i are the external radiative decay rate and internal loss rate of the resonance, respectively. The effects of the background dielectric constants, that is, ε_1 and ε_2 in eq 2, and the substrate mirror are reflected in these coupled-mode parameters, which are listed in Table 1

Table 1. Parameters in Eq 5 for the Emissivity Spectra in Figures 2 and 4b (Last Row)

No. of layers (N)	ω_0 (10^{14} rad/s)	γ_r (10^{12} rad/s)	γ_i (10^{12} rad/s)
1	2.594	0.049	0.471
2	2.605	0.095	0.471
3	2.614	0.138	0.471
4	2.623	0.179	0.471
5	2.632	0.218	0.471
6	2.640	0.256	0.471
graphene	2.598	2.842	4.811

for all emissivity spectra in Figure 2a. We see that the monolayer emitter is in an under-coupled state when $\gamma_r < \gamma_i$. The internal loss rate of the resonance is largely independent of the geometric parameters such as the width of the ribbon. As has been shown in refs 29 and 30 for these deep subwavelength resonances, the internal decay rate is approximately equal to half of the damping rate of the material resonance, that is, $\gamma_i \approx \gamma_\perp/2 = 0.471 \times 10^{12}$ rad/s. As N increases, the emitter volume increases and thus γ_r increases significantly, approaching γ_i. Therefore, as N increases, the emitter gradually approaches the critical coupling condition $\gamma_r = \gamma_i$, and hence, the emissivity peak reaches unity based on eq 5. A similar thickness dependence of the absorptivity also occurs in thin semiconductors.[31] The fact that the atomic layer is in the undercoupling condition makes it possible to enhance the emissivity by enhancing γ_r. In the Supporting Information, we show one way of enhancing γ_r by bringing the ribbons closer following the method discussed in ref 32. In doing so, we indeed can observe increases in the peak emissivity. The narrow band thermal radiation, as described in eq 5, indicates enhanced temporal coherence. We note, however, that such an emitter remains a thermal source. The photon quantum statistics is not influenced by the photonic designs here.

The peak emissivity shifts as we increase the number of atomic layers. We can understand this shift from Figure 2b, where we show the mode index of thin hBN film with different numbers of atomic layers. We see that the mode index decreases significantly as N increases, especially in the small N limit. Therefore, the resonance wavelength shifts to a shorter wavelength as N increases in order for eq 4 to be satisfied. In Figure 2c we show the mode index at the peak emissive wavelength. We see a clear stepwise change of the mode index as the atomic layer thickness, especially for small $N < 4$,
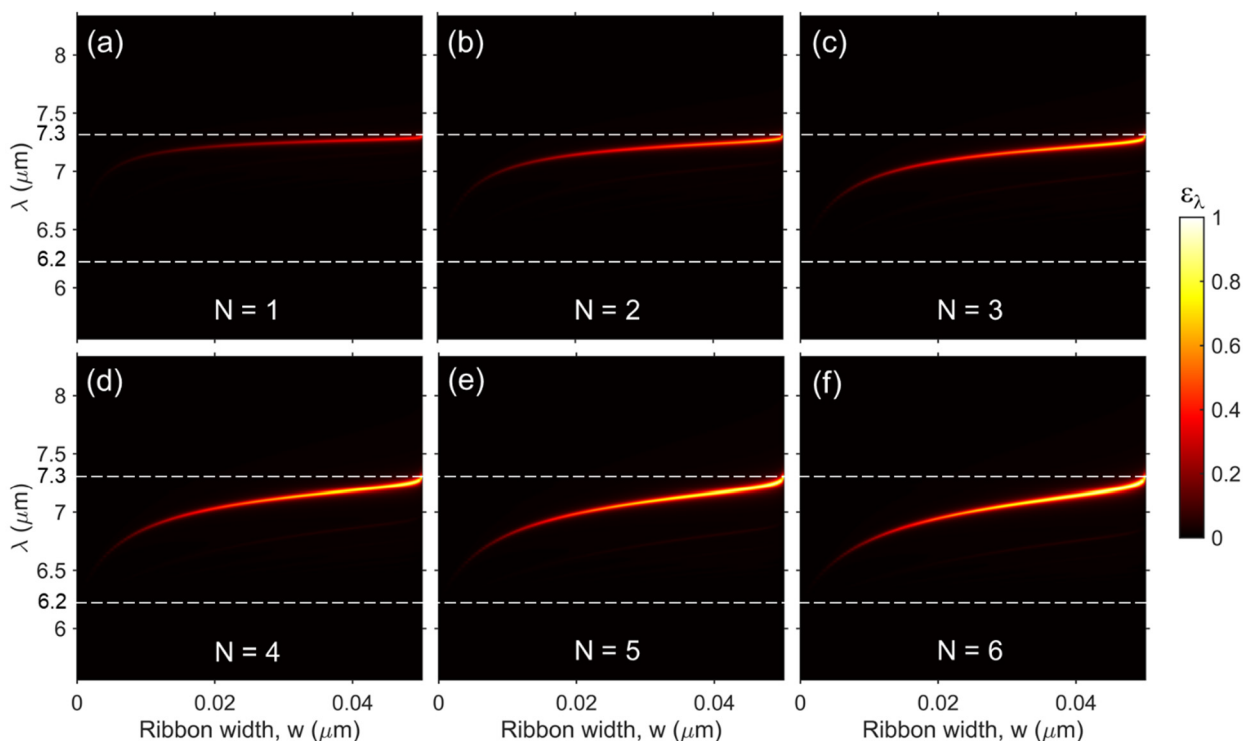

Figure 3. Emissivity as a function of wavelength and ribbon width for different numbers of hBN atomic layers.
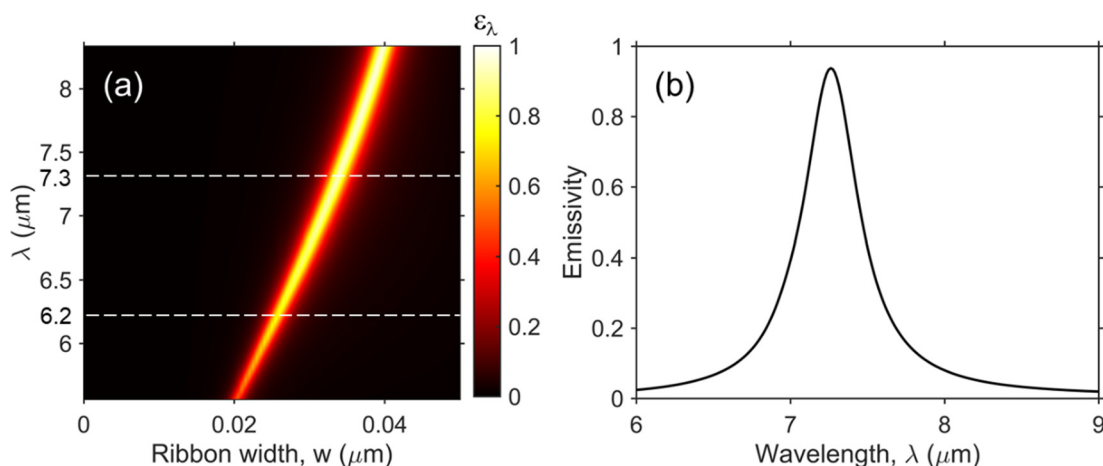
Figure 4. Emissivity of an emitter based on a graphene monolayer with a chemical potential of 0.28 eV.[35] The structure of the emitter is the same as the $N = 1$ case in Figure 2, except that $w = 0.0335$ μm.
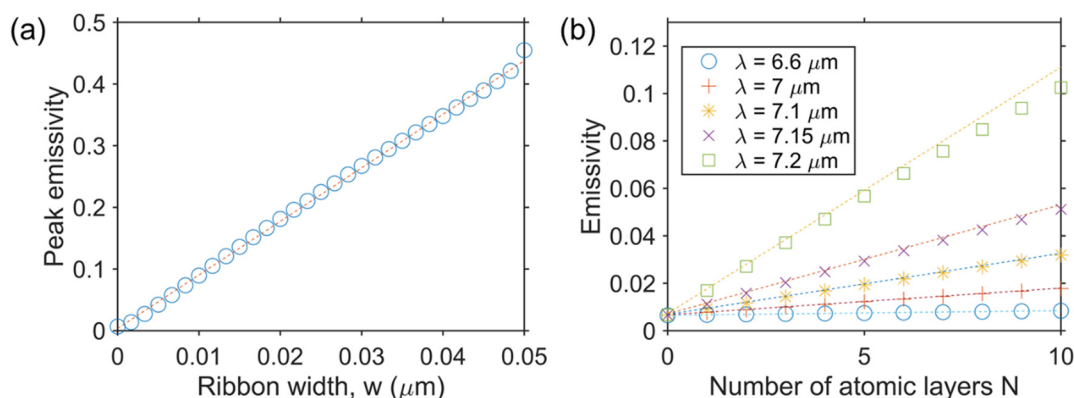

Figure 5. (a) Open circles show the dependence of the peak emissivity on ribbon width for the emitters discussed in Figure 3a. The dashed line is a linear fitting. (b) The emissivity at different wavelengths when N changes. The dashed lines are predictions from eq 6, in which we assume all lines pass through the emissivity point at $N = 0$.

indicating the atomic controllability of the phonon polariton ribbon mode.

Besides the atomic-scale dependence on the thickness, the emissivity is also extremely sensitive to the ribbon width. In Figure 3, we show the emissivity as a function of the wavelength and the ribbon width for different N. The bright bands are the fundamental order of the ribbon mode. For all cases, we see a clear dependence of the coherent emission peak on the ribbon width. The peak emissivity again increases as N increases for a fixed w. Therefore, the ribbon width and the thickness provide two degrees of freedom to precisely control the coherent emission. We note that, when $w = \Lambda$, that is, the hBN ribbon layer becomes a continuous film, the ribbon resonances transition to an epsilon-near-pole mode[33] at the transverse phonon wavelength ($\lambda = 7.3$ μm). The emissivity spectra from the ribbon modes and the epsilon-near-pole mode both have weak dependency as a function of angle, as shown in the Supporting Information, indicating a weak spatial coherence. But the frequency of the epsilon-near-pole mode is mostly determined by the material dielectric properties alone, and hence, it lacks the flexibility for tuning, in contrast with the ribbon resonances.

The ribbon resonances can also occur in plasmonic 2D materials such as doped graphene. In Figure 4, we show the emissivity of a graphene ribbon emitter based on the same structure as in Figure 1. In the Supporting Information, we

show that the ribbon resonance model in eq 4 can predict the peak emissivity of this graphene emitter very well. In general, compared to single-layer hBN emitters in Figure 3a, graphene ribbon resonances can provide a much higher peak emissivity. For example, Figure 4b shows a specific case where the wavelength of the emissivity peak is the same as the $N = 1$ case in Figure 2. Based on eq 5, we obtain the intrinsic and radiative loss rates of this emissivity spectrum (Table 1), from which we see that γ_r and γ_i are much closer to each other than the hBN emitter, making the graphene emitter closer to the critical coupling condition. However, since both γ_r and γ_i are significantly larger than those of the hBN emitter, the quality factor of the emissivity spectrum (16.5) is much lower than the hBN emitter (242.2). Similar quality factors were also reported in disk graphene resonators.[34]

Besides the atomic sensitivity of the emissivity, the radiative properties in the atomic scale also show a linear scaling with the ribbon width and number of layers. In Figure 5a, we show the peak emissivity for the emitters in Figure 3a as a function of the ribbon width. The dashed line in Figure 5a is a linear fit, which describes the trend very well. This linear scaling can be understood from the coupled-mode theory. As shown in Table 2, the radiative decay rate γ_r increases nearly linearly as the ribbon width increases. Since the internal decay rate is significantly larger than the radiative decay rate, the linear scaling of the radiative decay rate results in the linear increase

Table 2. Parameters in Eq 5 for the Emitters in Figure 5a

ribbon width (w, nm)	ω_0 (10^{14} rad/s)	γ_r (10^{12} rad/s)	γ_i (10^{12} rad/s)
10	2.642	0.010	0.463
15	2.623	0.016	0.465
20	2.613	0.022	0.467
25	2.606	0.029	0.469
30	2.601	0.035	0.470
35	2.597	0.042	0.471

of the peak emissivity based on eq 5. As shown in Table 1, a similar linear scaling of γ_r also applies when the number of layers N increases. However, since the radiative decay rate becomes comparable to the internal decay rates as N increase, the peak emissivity in this case does not scale linearly with N, as shown in Figure 2. On the other hand, if one considers wavelengths away from the emissivity peak, the denominator in eq 5 becomes roughly independent from the change of the thickness due to the $\omega - \omega_0$ term, and in this case the emissivity again follows a linear scaling law. In Figure 5b, we show this linearity in the case when the hBN layer is a continuous film such that the emissivity peak is fixed at the transverse phonon-polariton wavelength ($\lambda = 7.3 \ \mu$m). We see that the emissivity at shorter wavelengths, that is, away from 7.3 μm, indeed scales

linearly as N increases. In the Supporting Information, we show a quantitative analysis for this scaling behavior and obtain that the emissivity scales as

$$\varepsilon_\lambda = \frac{8\pi}{\lambda} \text{Im}(\varepsilon_\perp) N a \tag{6}$$

In Figure 5b, we plot the predictions of eq 6, which agree well with the direct calculations. The calculations start to deviate from the predicted linear trend at a large thickness for $\lambda = 7.2 \ \mu$m since it is too close to the transverse phonon wavelength.

The linear scaling when operating at the atomic scale provides some interesting opportunities to combine resonators with different sizes. We consider a case where we place two ribbon resonators with different sizes in one period, as shown in Figure 6a. When the ribbons are not too close such that the coupling is not significant, the structure has an emissivity spectrum with two peaks, each of which corresponds to the resonance frequency of a single ribbon. By tailoring the width of the two ribbons, one can therefore tailor the emission bandwidth. Meanwhile, due to the above-mentioned linearity of the emissivity, the sum of the peak emissivity values roughly stays the same for different hybrid emitters provided that
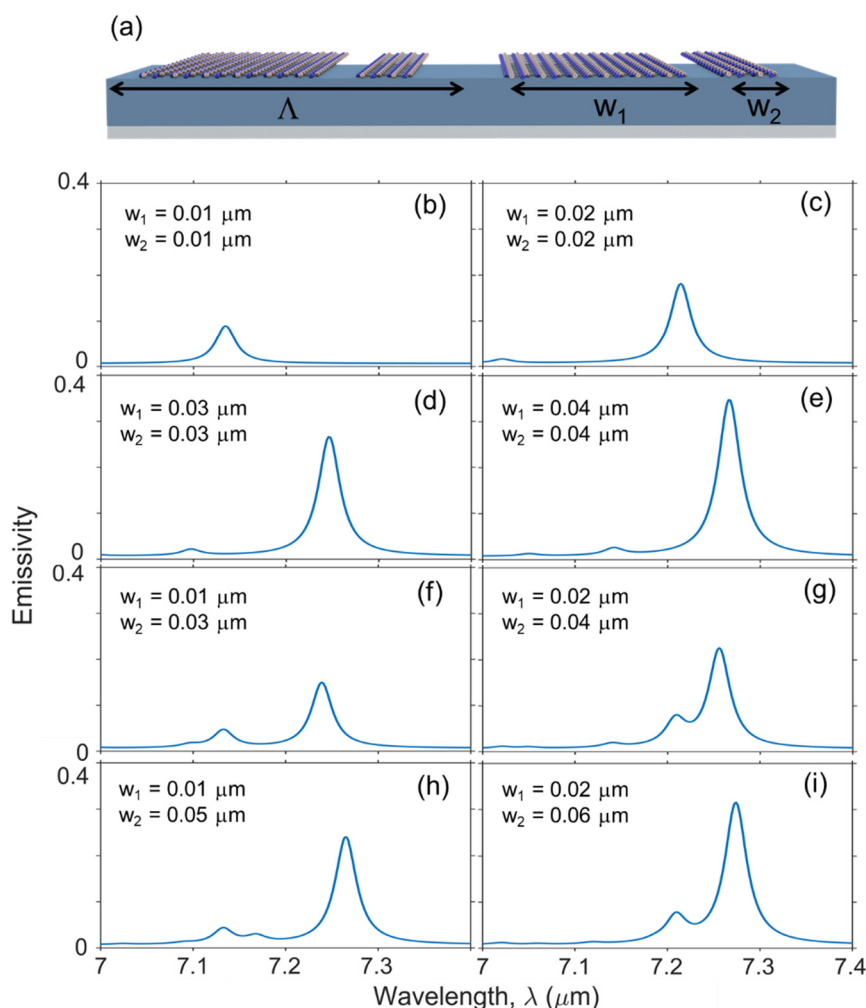

Figure 6. (a) Schematic of the nanophotonic thermal emitter that contains two hBN ribbon resonators in one period. The spacing between the two ribbons is $(\Lambda - w_1 - w_2)/2$. We use $\Lambda = 100$ nm. (b–i) Emissivity spectrum with different w_1 and w_2 combinations. The values of the w_1 and w_2 are noted on the plot.
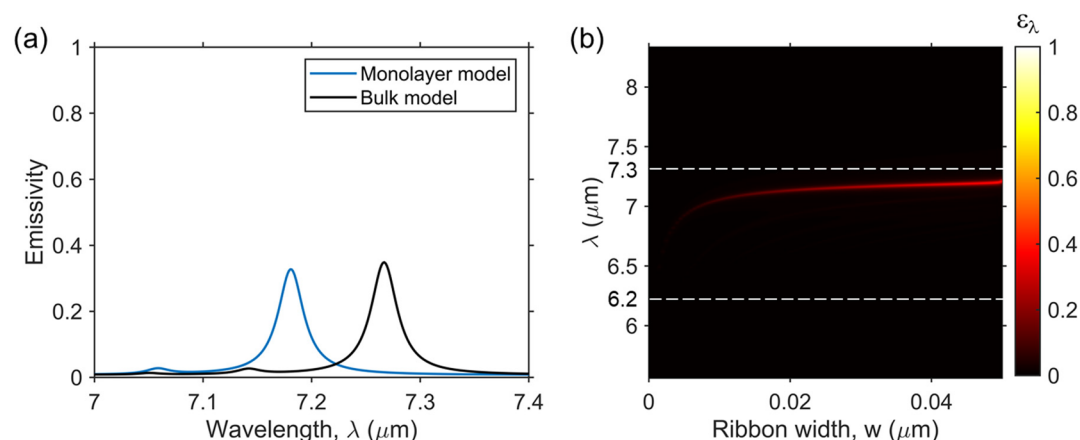
Figure 7. (a) Emissivity spectrum of a single layer hBN ribbon emitter using bulk and monolayer model for the dielectric function of hBN. The emitter has the same geometries as the N = 1 case in Figure 2. (b) The emissivity control using monolayer model of hBN. The emitters have the same geometries as the case in Figure 3a.

magnitude of $w_1 + w_2$ is maintained, as can be seen from comparing Figure 6d with h or Figure 6e with i.

As a final remark, we note that there are some recent studies pointing out that the dielectric function of hBN in the monolayer limit may be different from the bulk model we used in this work. The surface conductivity of monolayer hBN from first-principle simulation is given by[36,37]

$$\sigma_{\text{hBN,mono}} = -i\frac{4\varepsilon_0\omega\omega_{\text{TO,mono}}\nu_g}{\omega_{\text{TO,mono}}^2 - \omega^2 - i\omega\gamma_{\text{mono}}} \quad (7)$$

where $\omega_{\text{TO,mono}} = 1387$ cm^{-1}, $\nu_g = 1.2 \times 10^{-4}c_0$ is the group velocity of the phonon, with c_0 being the speed of light in vacuum, and $\gamma_{\text{mono}} = 5$ cm^{-1}. The equivalent dielectric function can be obtained from eq 3. We note that the group velocity of the phonon depends on its wave vector. The wave vector of the phonon polariton (β in eq 2) in our ribbon resonators are all smaller than 1 nm^{-1} (see Supporting Information for plots of β), in which range the group velocity can be treated as the above-mentioned constant without involving the nonlocal effect. In this monolayer limit, the LO phonon and TO phonon splitting disappears, and one ends up with a single phonon mode at a frequency near the TO phonon mode. The phonon mode frequency also slightly shifts to shorter wavelengths compared to the bulk model. In Figure 7a, we show the emissivity of the single-layer hBN ribbon emitter based on the monolayer model and the bulk model. Figure 7b illustrates the emissivity as the ribbon width changes, to be compared to Figure 3a. From these results, we clearly see the difference in the emissivity spectrum using the two models, but all major features of the emissivity spectra stay the same. Therefore, if one uses the monolayer model, the ribbon modes in the atomically thin emitters would shift slightly to shorter wavelengths. However, all major conclusions from calculations with the bulk model still hold.

In conclusion, we show that 2D materials, especially 2D phononic materials, provide an effective platform for controlling coherent thermal radiation with atomic precision. The radiative properties show unique linear scaling laws due to the low radiative decay rates of atomic resonators. Since 2D materials in general can be easily tuned using methods such as strain and gating,[38] our findings could open the possibilities for precise control and tuning of thermal radiation and could

benefit applications where thermal radiation control with emitters of a small footprint is needed.[39]

■ ASSOCIATED CONTENT

ⓢ Supporting Information

The Supporting Information is available free of charge at https://pubs.acs.org/doi/10.1021/acsphotonics.0c01879.

> Dielectric function of hBN and graphene, plasmon–polariton and phonon–polariton ribbon resonance, angular dependence of the ribbon resonance and the epsilon-near-pole resonance, scaling law of emissivity, and dielectric function of the monolayer model (PDF)

■ AUTHOR INFORMATION

Corresponding Authors

Mark Brongersma − *Department of Materials Science and Engineering, Geballe Laboratory for Advanced Materials, Stanford University, Stanford, California 94305, United States*; Email: markb29@stanford.edu

Shanhui Fan − *Department of Electrical Engineering, Ginzton Laboratory, Stanford University, Stanford, California 94305, United States;* ⓞ orcid.org/0000-0002-0081-9732; Email: shanhui@stanford.edu

Authors

Bo Zhao − *Department of Electrical Engineering, Ginzton Laboratory, Stanford University, Stanford, California 94305, United States;* ⓞ orcid.org/0000-0002-3648-6183

Jung-Hwan Song − *Department of Materials Science and Engineering, Geballe Laboratory for Advanced Materials, Stanford University, Stanford, California 94305, United States*

Complete contact information is available at:
https://pubs.acs.org/10.1021/acsphotonics.0c01879

Notes

The authors declare no competing financial interest.

■ REFERENCES

(1) Planck, M. *The Theory of Heat Radiation*; Forgotten Books: London, 2013.

(2) Hesketh, P. J.; Zemel, J. N.; Gebhart, B. Organ Pipe Radiant Modes of Periodic Micromachined Silicon Surfaces. *Nature* 1986, *324* (6097), 549−551.

(3) Greffet, J.-J.; Carminati, R.; Joulain, K.; Mulet, J.-P.; Mainguy, S.; Chen, Y. Coherent Emission of Light by Thermal Sources. *Nature* 2002, *416* (6876), 61−64.

(4) Fan, S. Thermal Photonics and Energy Applications. *Joule* 2017, *1* (2), 264−273.

(5) Zhang, Z. M. *Nano/Microscale Heat Transfer*; McGraw-Hill: New York, 2007.

(6) Wang, B.; Liu, M.; Huang, T.; Zhao, C. Micro/Nanostructures for Far-Field Thermal Emission Control: an Overview. *ES Energy Environ.* 2019, *6*, 18−38.

(7) Baranov, D. G.; Xiao, Y.; Nechepurenko, I. A.; Krasnok, A.; Alù, A.; Kats, M. A. Nanophotonic Engineering of Far-Field Thermal Emitters. *Nat. Mater.* 2019, *18* (9), 920−930.

(8) Li, W.; Fan, S. Nanophotonic Control of Thermal Radiation for Energy Applications. *Opt. Express* 2018, *26* (12), 15995−16021.

(9) Li, J.; Yu, B.; Shen, S. Scale Law of Far-Field Thermal Radiation from Plasmonic Metasurfaces. *Phys. Rev. Lett.* 2020, *124* (13), 137401.

(10) Naumis, G. G.; Barraza-Lopez, S.; Oliva-Leyva, M.; Terrones, H. Electronic and Optical Properties of Strained Graphene and Other Strained 2D materials: a Review. *Rep. Prog. Phys.* 2017, *80* (9), 096501.

(11) Liu, X.; Kang, J.-H.; Yuan, H.; Park, J.; Kim, S. J.; Cui, Y.; Hwang, H. Y.; Brongersma, M. L. Electrical Tuning of a Quantum Plasmonic Resonance. *Nat. Nanotechnol.* 2017, *12* (9), 866−870.

(12) Starko-Bowes, R.; Wang, X.; Xu, Z.; Pramanik, S.; Lu, N.; Li, T.; Jacob, Z. High-Temperature Polaritons in Ceramic Nanotube Antennas. *Nano Lett.* 2019, *19* (12), 8565−8571.

(13) Kumar, A.; Low, T.; Fung, K. H.; Avouris, P.; Fang, N. X. Tunable Light−Matter Interaction and the Role of Hyperbolicity in Graphene−hBN System. *Nano Lett.* 2015, *15* (5), 3172−3180.

(14) Gil, B.; Cassabois, G.; Cusco, R.; Fugallo, G.; Artus, L. Boron Nitride for Excitonics, Nano Photonics, and Quantum Technologies. *Nanophotonics* 2020, *9* (11), 3483−3504.

(15) Zhao, B.; Zhang, Z. M. Strong Plasmonic Coupling between Graphene Ribbon Array and Metal Gratings. *ACS Photonics* 2015, *2* (11), 1611−1618.

(16) Shi, Y.; Li, W.; Raman, A.; Fan, S. Optimization of Multilayer Optical Films with a Memetic Algorithm and Mixed Integer Programming. *ACS Photonics* 2018, *5* (3), 684−691.

(17) Wang, L. P.; Basu, S.; Zhang, Z. M. Direct and Indirect Methods for Calculating Thermal Emission From Layered Structures With Nonuniform Temperatures. *J. Heat Transfer* 2011, *133* (7), 072701−7.

(18) Dai, S.; Fei, Z.; Ma, Q.; Rodin, A. S.; Wagner, M.; McLeod, A. S.; Liu, M. K.; Gannett, W.; Regan, W.; Watanabe, K.; Taniguchi, T.; Thiemens, M.; Dominguez, G.; Neto, A. H. C.; Zettl, A.; Keilmann, F.; Jarillo-Herrero, P.; Fogler, M. M.; Basov, D. N. Tunable Phonon Polaritons in Atomically Thin van der Waals Crystals of Boron Nitride. *Science* 2014, *343* (6175), 1125−1129.

(19) Shin, H.; Yanik, M. F.; Fan, S.; Zia, R.; Brongersma, M. L. Omnidirectional Resonance in a Metal−Dielectric−Metal Geometry. *Appl. Phys. Lett.* 2004, *84* (22), 4421−4423.

(20) Vakil, A.; Engheta, N. Transformation Optics Using Graphene. *Science* 2011, *332* (6035), 1291−1294.

(21) Du, L.; Tang, D.; Yuan, X. Edge-Reflection Phase Directed Plasmonic Resonances on Graphene Nanostructures. *Opt. Express* 2014, *22* (19), 22689−22698.

(22) Nikitin, A. Y.; Low, T.; Martin-Moreno, L. Anomalous Reflection Phase of Graphene Plasmons and its Influence on Resonators. *Phys. Rev. B: Condens. Matter Mater. Phys.* 2014, *90* (4), 041407.

(23) Bozhevolnyi, S. I.; Søndergaard, T. General Properties of Slow-Plasmon Resonant Nanostructures: Nano-Antennas and Resonators. *Opt. Express* 2007, *15* (17), 10869−10877.

(24) Barnard, E. S.; White, J. S.; Chandran, A.; Brongersma, M. L. Spectral Properties of Plasmonic Resonator Antennas. *Opt. Express* 2008, *16* (21), 16529−16537.

(25) Chandran, A.; Barnard, E. S.; White, J. S.; Brongersma, M. L. Metal-Dielectric-Metal Surface Plasmon-Polariton Resonators. *Phys. Rev. B: Condens. Matter Mater. Phys.* 2012, *85* (8), 085416.

(26) Fan, S.; Suh, W.; Joannopoulos, J. D. Temporal Coupled-Mode Theory for the Fano Resonance in Optical Resonators. *J. Opt. Soc. Am. A* 2003, *20* (3), 569−572.

(27) Piper, J. R.; Fan, S. Total Absorption in a Graphene Monolayer in the Optical Regime by Critical Coupling with a Photonic Crystal Guided Resonance. *ACS Photonics* 2014, *1* (4), 347−353.

(28) Zhao, Z.; Guo, C.; Fan, S. Connection of Temporal Coupled-Mode-Theory Formalisms for a Resonant Optical System and its Time-Reversal Conjugate. *Phys. Rev. A: At., Mol., Opt. Phys.* 2019, *99* (3), 033839.

(29) Wang, F.; Shen, Y. R. General Properties of Local Plasmons in Metal Nanostructures. *Phys. Rev. Lett.* 2006, *97* (20), 206806.

(30) Raman, A.; Shin, W.; Fan, S. Upper Bound on the Modal Material Loss Rate in Plasmonic and Metamaterial Systems. *Phys. Rev. Lett.* 2013, *110* (18), 183901.

(31) Park, J.; Kang, J.-H.; Vasudev, A. P.; Schoen, D. T.; Kim, H.; Hasman, E.; Brongersma, M. L. Omnidirectional Near-Unity Absorption in an Ultrathin Planar Semiconductor Layer on a Metal Substrate. *ACS Photonics* 2014, *1* (9), 812−821.

(32) Zhao, N.; Zhao, Z.; Williamson, I. A. D.; Boutami, S.; Zhao, B.; Fan, S. High Reflection from a One-Dimensional Array of Graphene Nanoribbons. *ACS Photonics* 2019, *6* (2), 339−344.

(33) Molesky, S.; Dewalt, C. J.; Jacob, Z. High Temperature Epsilon-Near-Zero and Epsilon-Near-Pole Metamaterial Emitters for Thermophotovoltaics. *Opt. Express* 2013, *21* (S1), A96−A110.

(34) Thongrattanasiri, S.; Koppens, F. H. L.; García de Abajo, F. J. Complete Optical Absorption in Periodically Patterned Graphene. *Phys. Rev. Lett.* 2012, *108* (4), 047401.

(35) Zhao, B.; Zhao, J. M.; Zhang, Z. M. Enhancement of Near-Infrared Absorption in Graphene with Metal Gratings. *Appl. Phys. Lett.* 2014, *105* (3), 031905.

(36) Sohier, T.; Gibertini, M.; Calandra, M.; Mauri, F.; Marzari, N. Breakdown of Optical Phonons' Splitting in Two-Dimensional Materials. *Nano Lett.* 2017, *17* (6), 3758−3763.

(37) Rivera, N.; Christensen, T.; Narang, P. Phonon Polaritonics in Two-Dimensional Materials. *Nano Lett.* 2019, *19* (4), 2653−2660.

(38) Brongersma, M. L. The Road to Atomically Thin Metasurface Optics. *Nanophotonics* 2020, *10* (1), 643−654.

(39) Atwater, H. A.; Davoyan, A. R.; Ilic, O.; Jariwala, D.; Sherrott, M. C.; Went, C. M.; Whitney, W. S.; Wong, J. Materials Challenges for the Starshot Lightsail. *Nat. Mater.* 2018, *17* (10), 861−867.